Deng et al. *NPG Asia Materials* (2022) 14:25
https://doi.org/10.1038/s41427-022-00373-9

NPG Asia Materials

ARTICLE Open Access

Controllable tuning of polymetallic Co-Ni-Ru-S-Se ultrathin nanosheets to boost electrocatalytic oxygen evolution

Wei Deng[1], Wenshuo Xie[1], Dan Li[1], Yuping Gai[1], Zhide Chen[1], Jun Yu[1], Renqiang Yang[2], Xichang Bao[2] and Fei Jiang[1]

Abstract

Replacing precious metals in oxygen evolution reaction (OER) catalysts has broad prospects to achieve a viable water splitting system. Since the electrocatalytic OER is a four-electron transfer reaction with a very sluggish kinetic process, there is great interest in the development of inexpensive, durable, and high-efficiency OER catalysts. Herein, trimetallic Co-Ni-Ru sulfoselenide and bimetallic sulfoselenide nanosheets were designed by regulating their composition and morphology for efficient and durable OER electrocatalysis. The sheet structure has a large specific surface area to promote contact between the catalyst and electrolyte. Compared with bimetallic Co-Ni, Co-Ru, Ni-Ru, Co-Cd, and Co-Au sulfoselenide nanosheets, trimetallic Co-Ni-Ru sulfoselenide nanosheets show superior OER performance. By modulating the composition ratio of metal atoms in the Co-Ni-Ru-S-Se nanosheets (1:1:0.5:1:1), the nanosheets showed a significant OER overpotential of $\eta = 261$ mV (1.491 V versus RHE) at 10 mA cm^{-2}, a Tafel slope of 52.2 mV dec^{-1} and outstanding stability after 48 h of continuous testing. For comparison, Co-Ni, Co-Ru, Ni-Ru, Co-Cd, and Co-Au bimetallic sulfoselenide nanosheets (denoted as Co-Ni-S-Se, Co-Ru-S-Se, Ni-Ru-S-Se, Co-Au-S-Se, Co-Cd-S-Se) were also tested. Density functional theory (DFT) calculations showed that appropriately doping Ru and Ni simultaneously (Co-Ni-Ru-S-Se) can increase the density of the states at the Fermi level, resulting in excellent charge density and low intermediate adsorption energy. These findings present a practical route to design 2D polymetallic nanosheets to optimize catalytic OER performance.

Introduction

Fossil fuels are nonrenewable energy sources that cause serious environmental pollution problems. This has stimulated researchers to search for and develop sustainable and clean energy sources in recent decades. Hydrogen produced by the electrocatalytic cracking of water is renewable and pollution-free[1–3]. At present, investigations have found that the oxygen evolution reaction (OER) mainly involves 4-electron transfer processes, which greatly hinders its kinetic process and limits its practical applications in electrocatalytic water splitting[4–6]. The rare noble metal oxides RuO_2 and IrO_2 are the benchmark electrocatalysts for oxygen evolution. However, their high cost, scarcity, and instability limit their practical applications in commercial aspects[7–9]. Hence, the development of low-cost base transition metal catalysts is in high demand and has urgent application value. Currently, a large number of oxygen evolution catalysts have been developed, such as transition metal oxides[10–12], hydro(oxy)oxides[13,14], sulfides[15,16], nitrides[17,18], and phosphides[19,20]. Among them, cobalt-based sulfides or selenides have attracted considerable attention due to their configurations to stimulate electrochemical-reacting surfaces[21–23]. Nevertheless, the low number of active sites

Correspondence: Dan Li (lidansit@163.com) or
Jun Yu (yujunhuazhong2002@126.com) or Fei Jiang (jiangfei@sit.edu.cn)
[1]School of Chemical and Environmental Engineering, Shanghai Institute of Technology, Shanghai 201418, China
[2]CAS Key Laboratory of Bio-based Materials, Qingdao Institute of Bioenergy and Bioprocess Technology, Chinese Academy of Sciences, Qingdao 266101, China

inhibit the OER process tremendously. Notably, some researchers have further improved the oxygen evolution performance of metal compounds by using multiple metal atoms[24–26]. For example, Wang prepared a unique heterostructure interdoped (Ru-Co)O_x hollow nanosheet array, which showed prominent electrocatalytic activity and durable stability during the OER[27]. Zhu and Liu presented the multi-transition metal selenide $CoNiSe_2$, which has an optimized number of Se vacancies and possesses improved OER properties, containing a low overpotential $\eta = 252\,mV$ at $10\,mA\,cm^{-2}$ and efficient stability after 30 h[28–31]. Zhao used a steerable synthesis strategy to optimize the composition of metal atoms, and the generated Co_4Ni_1P nanotubes showed significant OER catalytic performance in alkaline electrolytes[32]. Zhuang used the plasma photochemical strategy to prepare the selenium vacancy of a single Pt atomic species[33]. This enhanced oxygen evolution performance was mainly ascribed to the dopant and host metal synergy between atoms. Nevertheless, a detailed explanation of the heterostructure cooperative effect remains obscure. Hence, it is vital to explain the electronic structure and properties of polymetallic sulfur–selenium compounds toward OER activity.

Two-dimensional nanostructured OER catalysts have controllable morphologies and novel structures owing to their various unique preparation processes[34–36]. Among the many two-dimensional nanostructured oxygen evolution catalysts, layered oxygen evolution catalysts can provide a larger specific surface area when in contact with the electrolyte, thereby greatly improving their electrocatalytic performance[37,38]. For example, Sun reported a universal ion exchange method to obtain Fe-doped Ni$(OH)_2$ and $Co(OH)_2$ nanomaterials and enhance the oxygen release reaction[39]. Du systematically analyzed progressive morphology modulation on MNMCs and applied them for electrocatalysis, strengthening the electrochemical properties of 0D, 1D, 2D, and 3D noble metal-based electrocatalysts for OERs and HERs[40–43]. Zhu developed the two-dimensional OER catalyst Fe_1Co_1-ONS. The oxygen vacancies generated in this material can increase the adsorption of H_2O to the Co^{3+} sites[44]. Consequently, ultrathin nanosheets can promote the mass transport of OH- ions and supply many active sites for catalysis.

Based on the above considerations, elaborate composition adjustments and morphology control were considered in the design of an OER catalyst to make full use of their respective advantages. Trimetallic Co-Ni-Ru-S-Se shows different molecular configuration transformations than bimetallic Co-Ni-S-Se, which exhibits differentiation of the atomic arrangements. In particular, the charge density of the original Co-Ni-Ru-Se or Co-Ni-Ru-S monolayer is evenly distributed and mainly concentrated in the center of the Co atom, while the observed difference in charge density of the Co-Ni-Ru-S alloy monolayer is partially due to the different electronegativities of the S and Se atoms. This may mainly be caused by the submission of half S (or Se) and Se (or S), so the concentric charge density of the Co atom reduces the d-orbital of the metallic Co atoms and the Se orbital, which is helpful for adjusting the d-band construction of the metal atoms. Herein, we demonstrate that trimetallic sulfoselenide (Co-Ni-Ru-S-Se) nanosheets are evenly distributed by using a liquid–liquid interface-mediated strategy (oleylamine and water as the two reaction media). In comparison with the utilization of monometallic Co-S-Se alone, the simultaneous polymetallic doping of Ru and Ni can enhance the OER performance, which is strongly associated with the molar ratio of Ru, Ni, and Co. In addition, trimetallic Co-Ni-Ru-S-Se nanosheets possess remarkable performance with an overpotential as low as 261 mV at $10\,mA\,cm^{-2}$, a Tafel slope of $52.2\,mV\,dec^{-1}$, and long-lasting stability after 48 h of continuous testing. The density functional theory (DFT) results show that the increase in the activity of Co-Ni-Ru-S-Se is due to an increase in the density of states (DOS) close to the Fermi level, thus leading to enhancement in the active polymetallic catalytic site.

Results and discussion

Morphologies and structures

To achieve highly electroactive ultrathin nanosheets for OERs, we elaborately designed trimetallic Co-M_1-M_2-S-Se and bimetallic Co-M_1-S-Se (M_1, M_2 denotes Ni or Ru or Cd or Au) composite materials that were based on the precursors cobalt (III) acetylacetonate ($Co(acac)_3$), sulfur powder (S) and selenium powder (Se). As depicted in Fig. 1a, the pristine trimetallic Co-Ni-Ru-S-Se and bimetallic Co-Ni-S-Se, Co-Ru-S-Se, Ni-Ru-S-Se, Co-Au-S-Se, and Co-Cd-S-Se materials were synthesized via a one-pot hydrothermal process in which $Co(acac)_3$ was used as the source of Co metal cations, S and Se powder were used as the controllable negative ions, and the other metal ions (Ru, Ni, Cd, Au) were used as dopants. By adjusting the molar ratios of the metal atoms Ni, Ru, Au, and Cd, the bimetallic Co-Ni-S-Se, Co-Ru-S-Se, Ni-Ru-S-Se, Co-Au-S-Se, and Co-Cd-S-Se and trimetallic Co-Ni-Ru-S-Se composite materials with tunable element components were accordingly optimized. The synthetic process with different ratios of bimetallic and trimetallic composite materials is detailed in the experimental methods. Herein, we focused on six products containing various chemical compositions: Co-Ni-S-Se, Co-Ru-S-Se, Ni-Ru-S-Se, Co-Au-S-Se, Co-Cd-S-Se, and Co-Ni-Ru-S-Se.

Typical low-resolution and high-resolution transmission electron microscopy (LRTEM and HRTEM) figures (Fig. 1b, c) showed that the as-prepared bimetallic Co-Ni-S-Se

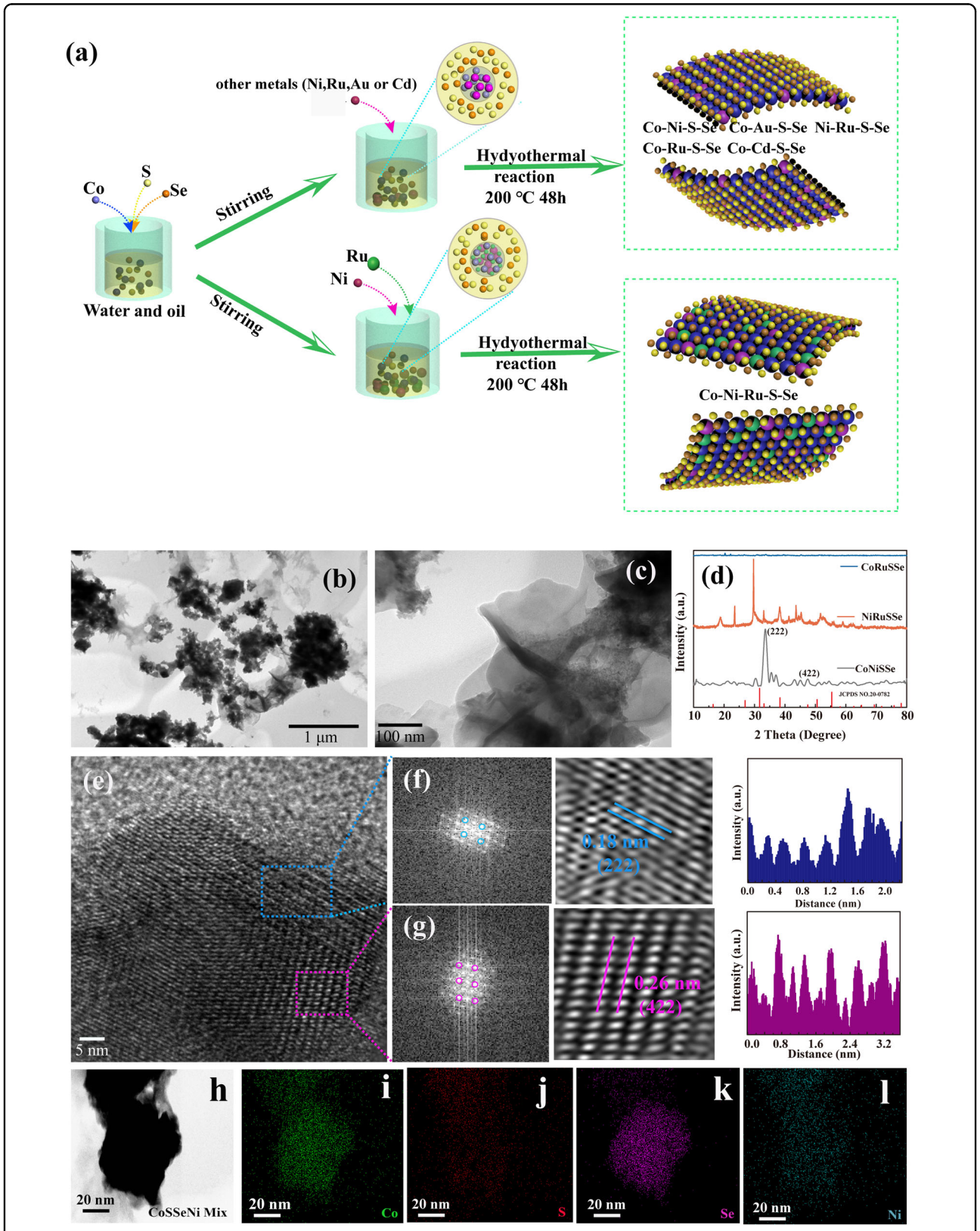

Fig. 1 Schematic illustration and morphology characterizations. a Schematic illustration of the synthetic process for Co-M_1-S-Se and Co-M_1-M_2-S-Se nanosheets at the oil/water interface. **b**, **c** TEM image for the Co-Ni-S-Se. **d** XRD of Co-Ni-S-Se, Ni-Ru-S-Se, Co-Ru-S-Se, standard $NiCo_2S_4$ card (PDF#20–0782). **e** HRTEM spectrum of Co-Ni-S-Se. **f**, **g** FFT and IFFT pattern of Co-Ni-S-Se. **h**–**l** HAADF-STEM spectrum with elemental mapping images for Co, Ni, S, and Se.

products were exclusively high-quality nanosheet structures. The robust crystalline nature of the Co-Ni-S-Se nanosheets was confirmed by X-ray diffraction (XRD), as shown in Fig. 1d. The peaks in the spectrum at ~32.3° and 47.4° were ascribed to the (222) and (422) facets, respectively, and were consistent with the standard $NiCo_2S_4$ card (PDF 20–0782). Figure 1e (marked blue and purple) displays the HRTEM spectrum of the Co-Ni-S-Se structure. Figure 1f shows lattice fringes with a distance of 0.18 nm, which correspond to the (222) plane of Co-Ni-S-Se. Figure 1g reveals a lattice fringe spacing of 0.26 nm (purple), which corresponds to the (422) facet of Co-Ni-S-Se. The energy dispersive X-ray (EDX) spectrum of the Co-Ni-S-Se nanosheet (Fig S1a) shows that the approximate composition ratio of Co, S, Se, and Ni was 1:1:1:0.5 (Co:S:Se:Ni). The Co-Ni-S-Se chemical molar ratio was determined to be $Co_{0.48}Ni_{0.22}S_{0.46}Se_{0.41}$ by inductively coupled plasma atomic emission spectrometry (ICP-AES). In addition, line scanning indicated that the elements Co, Ni, S, and Se were evenly dispersed in the Co-Ni-S-Se samples (Fig. S1b–h). Through high-angle annular dark-field scanning transmission electron microscopy (HAADF-STEM), the spatial distribution of different elements located on the nanosheets was confirmed (Fig. 1h). The corresponding EDX mapping image shows that Co, Ni, S, and Se are homogeneously dispersed onto the entire Co-Ni-S-Se nanosheet (Fig. 1i–l).

Figure 2a schematically illustrates the molecular configuration transformations from bimetallic Co-Ni-S-Se to trimetallic Co-Ni-Ru-S-Se, which exhibits differentiation of the atomic arrangements from three different perspectives. The scanning electron microscopy (SEM) image in Fig. 2b distinctly illustrates that the as-prepared trimetallic Co-Ni-Ru-S-Se also possesses a typical sheet-like structure, and the corresponding EDX spectrum proved the homogeneous distribution of Co, S, Se Ni, and Ru atoms in the samples (Fig. S2). The HRTEM images shown in Fig. 2c and Fig. 2d also demonstrate the sheet-like structure of the Co-Ni-Ru-S-Se products. The crystal structures of the materials were determined by X-ray diffraction (XRD), as shown in Fig. 2e. A peak at ~34.6° originates from the (210) plane of Co-Ni-Ru-S-Se. The characteristic diffraction peaks of Co-Ni-Ru-S-Se at ~52.4° and 49.4° are consistent with the (222) and (311) crystal planes. Figure 2f g displays the HRTEM images of the Co-Ni-Ru-S-Se sample, accompanied by the FFT patterns and IFFT patterns of the selected areas. Figure 2f reveals lattice fringe spacings of 0.20 nm and 0.14 nm, which correspond to the (400) and (220) facets of Co-Ni-Ru-S-Se. Figure 2g shows lattice fringes with distances of 0.30 nm and 0.18 nm, which have been assigned to the (222) and (311) planes of Co-Ni-Ru-S-Se. The corresponding elemental mappings further indicate that the constituent Co, Ni, S, Se, and Ru elements of Co-Ni-Ru-S-Se (Fig. 2h–l) were evenly distributed throughout the whole catalyst matrix. EDX spectroscopy showed that the molar ratio of Co, Ni, and Ru in the as-prepared Co-Ni-Ru-S-Se sample was close to 0.25:0.2:0.05 (Fig. S3), which corresponded to an approximate composition ratio of Co, Ni, Ru, S and Se of $Co_{0.31}Ni_{0.22}Ru_{0.05}S_{0.46}Se_{0.41}$ by ICP-AES.

Chemical valance states

Atomic force microscopy (AFM) further confirmed the ultrathin nanosheet morphology of Co-Ni-Ru-S-Se with an average thickness of 0.92 nm (Fig. 3a). To identify the changes in chemical composition and element valence of Co-Ni-Ru-S-Se, Co-Ru-S-Se, and Co-Ni-S-Se, X-ray photoelectron spectroscopy (XPS) analysis was performed. The results are shown in Fig. 3b–f and Fig. S4. The full XPS spectrum (Fig. 3b) revealed that the Co-Ni-Ru-S-Se sample was composed of the elements Co, S, Se, Ru, and Ni, which was consistent with the EDS analysis. Specifically, in the XPS spectrum, the Co 2p, Ni 2p, Ru 3p and Se 3d districts were split into two doublets owing to spin-orbit coupling. In Fig. 3c, the Co $2p_{3/2}$ spectrum showed 2 spin-orbit peaks (Co $2p_{1/2}$ and Co $2p_{3/2}$), and the Co $2p_{3/2}$ peak could be ascribed to Co(III) (777.94 eV) and Co(II) (781.97 eV); these peaks were accompanied by a satellite peak (786.32 eV), which could be assigned to the Co in Co-Ni-Ru-S-Se[45,46]. Furthermore, the 3d spectrum of Se (Fig. 3d) displayed peaks at 53.2 eV (Se $3d_{5/2}$) and 54.3 eV (Se $3d_{3/2}$). A peak at 58.7 eV resulted from a SeO_x species owing to exposure to air. Moreover, the Ni 2p peaks in Fig. 3e were designated at 855.6 and 874.1 eV, which are in accordance with Ni $2p_{3/2}$ and Ni $2p_{1/2}$ in Co-Ni-Ru-S-Se, respectively[47,48]. The 3p spectrum of Ru displayed in Fig. 3f exhibited a Ru $3p_{3/2}$ peak from Co-Ni-Ru-S-Se, which could be assigned to a Ru (IV) (461.12 eV) peak and a satellite peak (464.76 eV)[27]. The value of H_{ads} is usually stronger in catalysts containing Ru sites[49,50]. while the O_{ads} value is weak, resulting in slow water splitting kinetics. Electronic regulation owing to the interfacial cooperative effect could endow Co-Ni-Ru-S-Se with enhanced catalytic activity toward water decomposition[51]. The Co 2p and Se 3d XPS spectra of Co-Ni-Ru-S-Se showed a slight shift compared with pure Co-Ru-S-Se and Co-Ni-S-Se, confirming a strong charge interaction relationship between Co-S-Se and the doped Ru Ni (Fig. 3c, d). Other XPS survey spectra, S 2p and Cd 3d, are depicted in Fig. S5. Compared with monodoped Co-Ru-S-Se and Co-Ni-S-Se, the dual-cation-doped Co-Ni-Ru-S-Se exhibited a more positive shift in the Co 2p and Se 3d binding energy, indicating charge transfer between the cations in the Co-Ni-Ru-S-Se catalyst.

OER electrocatalytic performance analyses

To survey the electrocatalytic performance of the prepared materials, a typical three-electrode system was

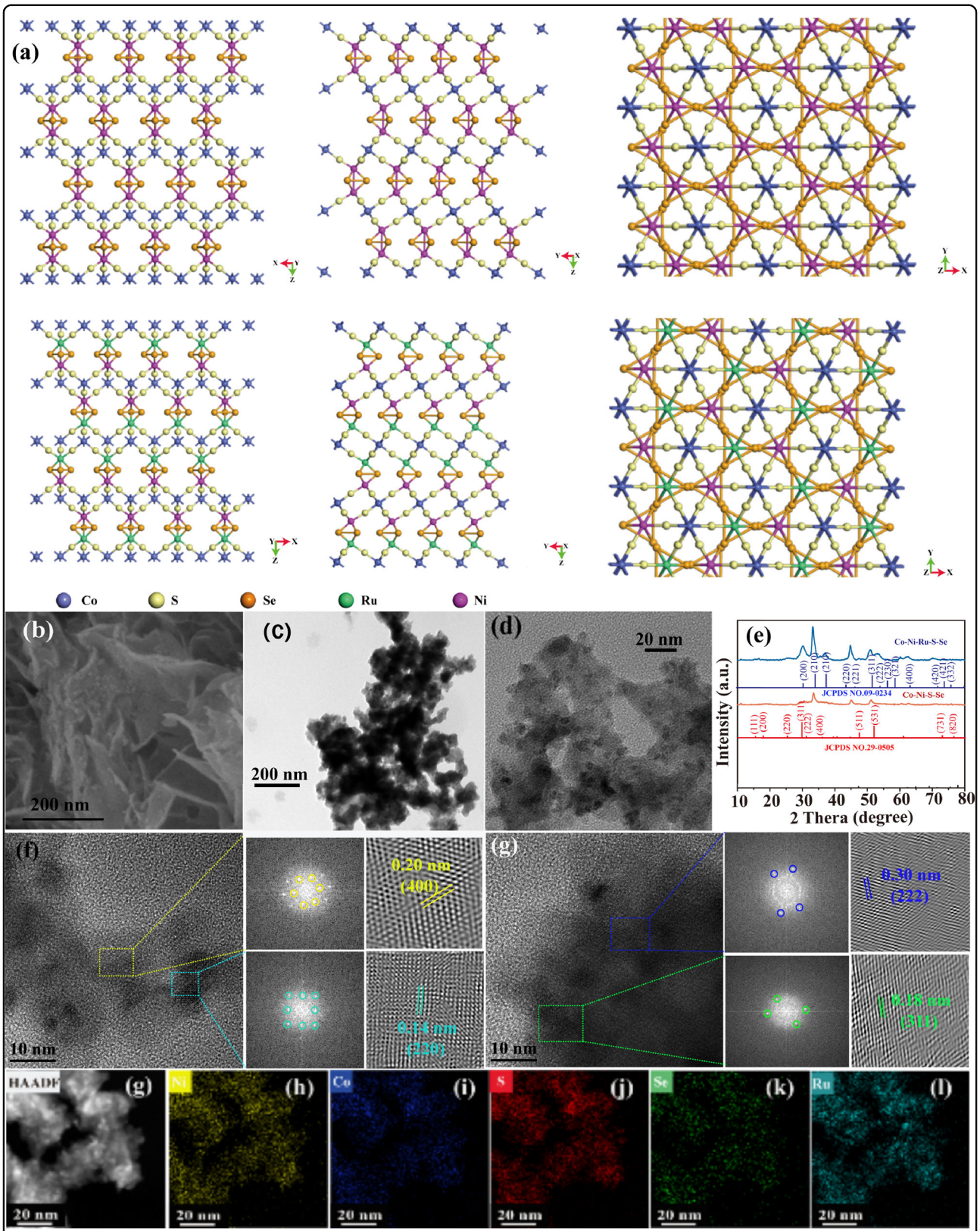

Fig. 2 Molecular models and morphology characterizations. a Schematically illustrated the bimetallic Co-Ni-S-Se and trimetallic Co-Ni-Ru-S-Se molecular configuration. **b** SEM images of Co-Ni-Ru-S-Se nanosheet. **c**, **d** TEM images of Co-Ni-Ru-S-Se. **e** XRD of Co-Ni-Ru-S-Se and Co-Ni-S-Se, standard $CoSe_2$ card (PDF#09–0234), standard $CuRu_2S_4$ card (PDF#29–0505). **f**, **g** HRTEM images of Co-Ni-Ru-S-Se of different selected areas. **h**–**l** HAADF-STEM images with elemental mapping for Co, S, Se, Ru, and Ni, respectively.

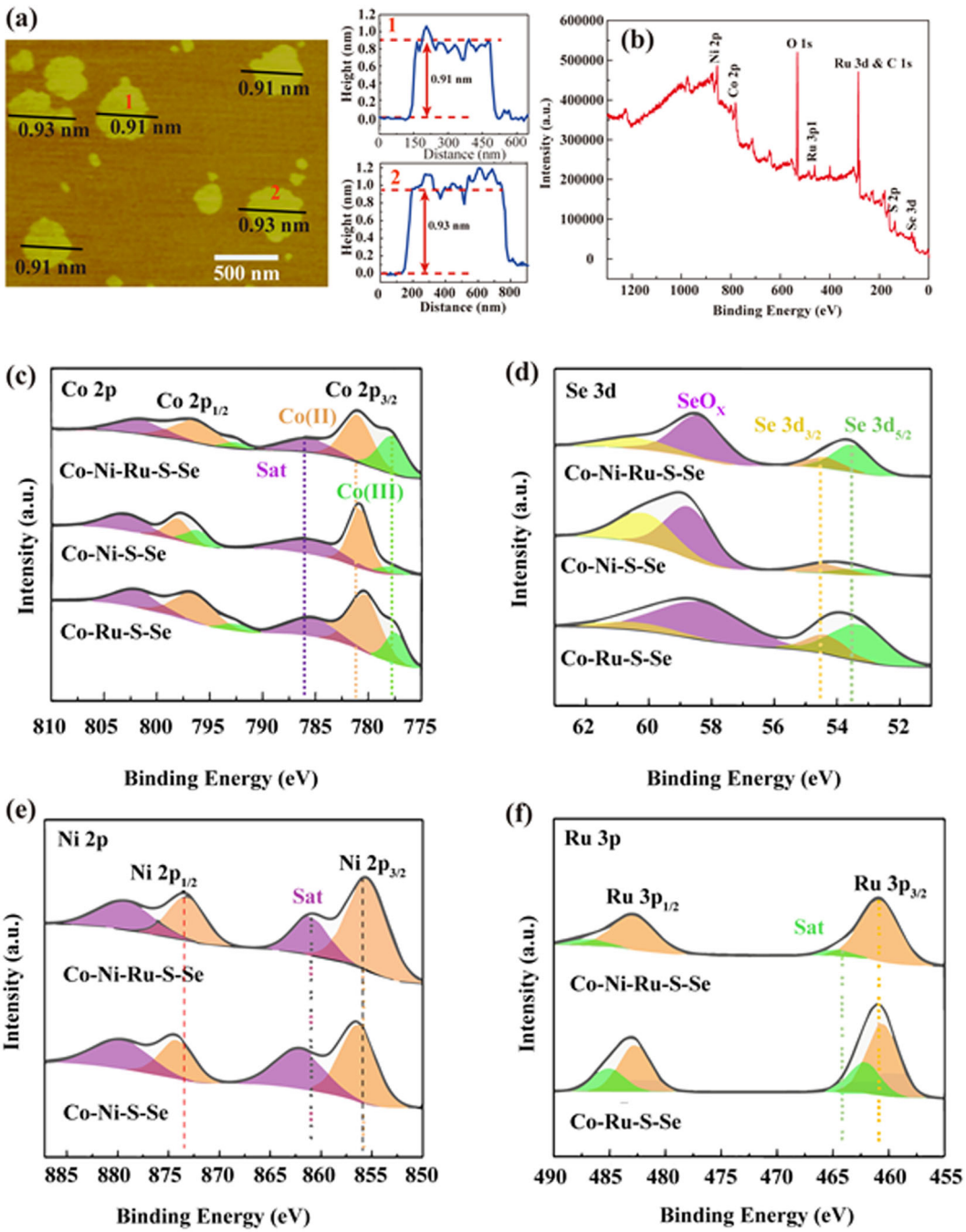

Fig. 3 Structural characterizations. a Atomic force microscopy spectrum, the corresponding height profiles (we note that the numbers from 1 and 2 in (**a**). **b** XPS spectra for Co-Ni-Ru-S-Se Survey. **c**–**f** XPS spectra of Co 2p, Se 3d, Ni 2p, and Ru 3p.

utilized to assess the OER properties of the polymetallic doping material in a 1 mol L^{-1} KOH solution[52,53]. For comparison, a marketed RuO_2 catalyst was also tested as a reference[54]. All potentials were transformed to a reversible hydrogen electrode (RHE). Figure 4a shows the linear sweep voltammetry (LSV) curves of the synthesized materials. Undoubtedly, the standard RuO_2 catalyst presented the best OER activity and was accompanied by the smallest potential of 1.484 V (vs. RHE), which was converted to an overpotential of $\eta_{10} = 254$ mV to obtain a 10 mA cm^{-2} current density. The Co-Ru-S-Se, Ni-Ru-S-Se, Co-Au-S-Se, and Co-Cd-S-Se nanomaterials displayed very

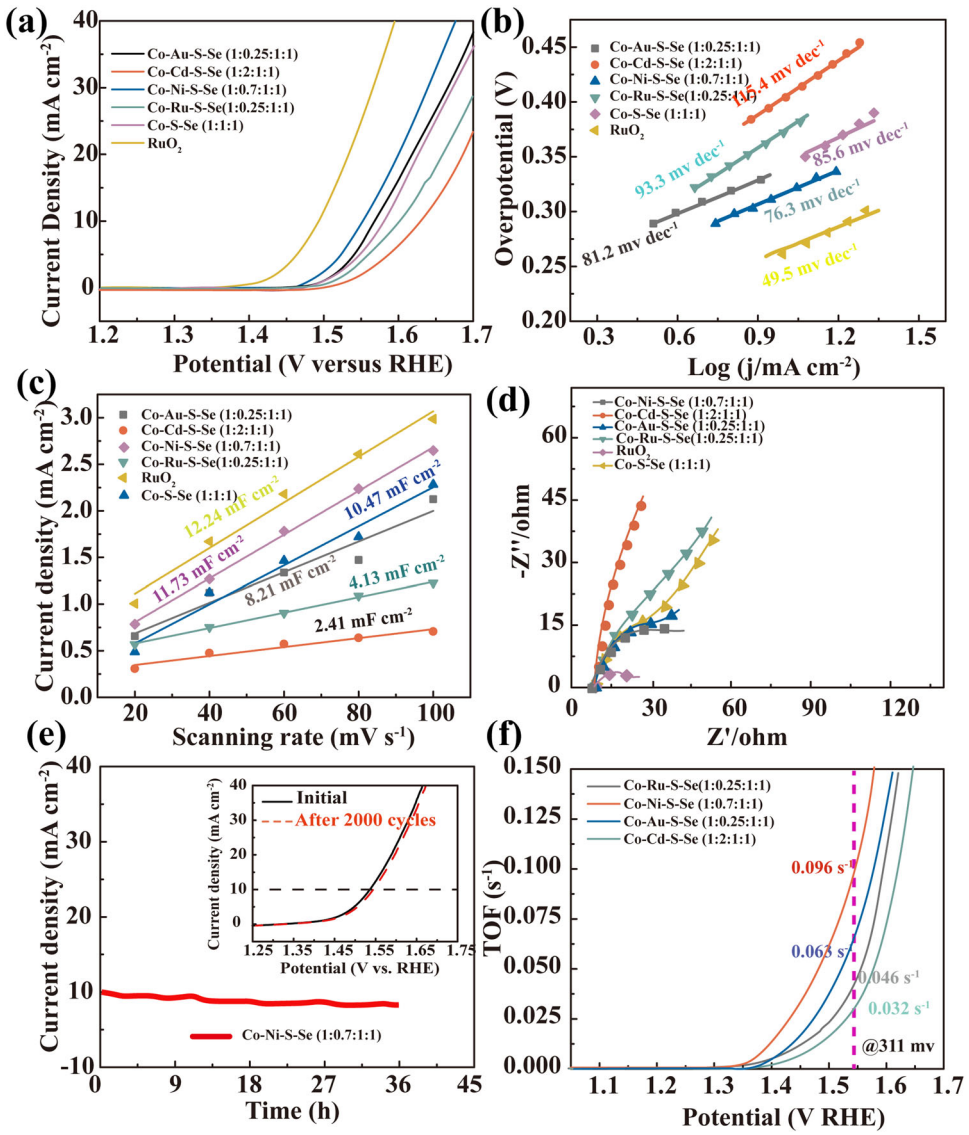

Fig. 4 Electrocatalytic OER performance of bimetallic nanosheets. a OER polarization curves, **b** Tafel plots of Co-Ru-S-Se, Co-Ni-S-Se, Co-Cd-S-Se, Co-Au-S-Se, RuO_2, and Co-S-Se. **c** C_{dl} values of current density differences plotted against scan rates of Co-Ru-S-Se, Co-Ni-S-Se, Co-Cd-S-Se, Co-Au-S-Se, RuO_2 and bare Co-S-Se. **d** EIS Nyquist plots of Co-Ru-S-Se, Co-Ni-S-Se, Co-Cd-S-Se, Co-Au-S-Se, RuO_2, and bare Co-S-Se. **e** Everlasting stability for the Co-S-Se at current densities of 10 mA cm^{-2} for 36 h, inset in (**e**) continuous CV scanning after 2000 circles at 100 mV s^{-1}. **f** TOF curves of Co-Ni-S-Se, Co-Cd-S-Se, Co-Au-S-Se, and Co-Ru-S-Se at the overpotential of 311 mV.

low OER activity with high overpotentials (360 mV, 392 mV, 323 mV, and 431 mV at 10 mA cm^{-2}, respectively) and weak current densities, while the Co-Ni-S-Se catalyst needed an overpotential of only 311 mV (Fig. 4a and Fig. S6). Determining the variation in Ni content among different metal-doped materials in the Co-M_1-S-Se family of electrocatalysts, which can be achieved by modulating various components, is important and has a significant influence on electrocatalytic performance. The Co-Ni-S-Se catalyst was found to be the best catalyst among all of the Co-M_1-S-Se samples. Specifically, the Co-Ni-S-Se catalyst required an overpotential of only 311 mV, which was better than those of Co-Cd-S-Se and Co-Au-S-Se. Tafel diagrams are generally used to survey and confirm faster OER kinetics[55]. The Co-Ni-S-Se nanosheets presented a Tafel slope of 76.3 mV dec^{-1} (Fig. 4b), which was noticeably superior to those of Co-Cd-S-Se (115.4 mV dec^{-1}), Co-Au-S-Se (81.2 mV dec^{-1}), and Co-Ru-S-Se (93.3 mV dec^{-1}). During the oxygen evolution process, the double-layer capacitance (C_{dl}) of the electrocatalyst is proportional to its electrochemically active surface area (ECSA)[56]. On the basis of the cyclic voltammograms (CVs) at various scan rates in

the non-Faradaic potential region (Fig. S7), the Co-Ni-S-Se catalyst exhibited a C_{dl} value of 11.73 mF cm^{-2} (Fig. 4c), which was remarkably larger than those of Co-Cd-S-Se (2.41 mF cm^{-2}), Co-Au-S-Se (8.21 mF cm^{-2}) and Co-S-Se (10.73 mF cm^{-2}). This result suggested that the Co-Ni-S-Se nanosheets possessed more active sites, providing a significant contribution to the enhanced OER performance. We also performed electrochemical impedance spectroscopy (EIS) measurements to obtain the electrode kinetics during the electrocatalytic OER process[57,58]. As surveyed from the Nyquist plots (Fig. 4d), the Co-Ni-S-Se catalyst possessed the smallest charge transfer resistance (R_{ct}) among all of the bimetallic family materials, presenting faster OER kinetics and an accelerated Faradaic process on the Co-Ni-S-Se electrode. This result further showed that the charge transfer process could be expedited by optimizing the Ni content in the Co-Ni-S-Se sample. The ECSA and EIS analytical results were both consistent with the excellent OER activity that the Co-Ni-S-Se nanosheets exhibited in the LSV curves. The stability of the as-fabricated Co-Ni-S-Se nanosheets was further evaluated through consecutive CV scanning for 2000 cycles and chronoamperometry measurements in a KOH solution. As indicated in Fig. 4e, the polarization curves after 2000 CV cycles still overlapped with the previous curve, demonstrating that the Co-Ni-S-Se catalyst has excellent electrocatalytic stability. The result in Fig. 4f clearly shows that when the overpotential was 311 mV, the turnover frequency (TOF) value of Co-Ni-S-Se was the largest (0.096 s^{-1}), which was three times that of Co-Cd-S-Se (0.032 s^{-1}). This phenomenon indicated that Ni doping had a great influence on the electrochemical properties.

Similarly, a typical three-electrode system was utilized to investigate the OER activity of the Co-Ni-Ru-S-Se catalyst in 1.0 mol L^{-1} KOH medium. The samples containing the optimized Co-Ni-S-Se catalysts were selected for comparison. Figure 5a shows LSV curves with a scan rate of 5 mV s^{-1}. The Co-Ni-Ru-S-Se (1:1:0.5:1:1) catalyst exhibited the best performance. The η_{10} of Co-Ni-Ru-S-Se (1:1:0.5:1:1) was 261 mV (1.491 V vs. RHE), which was noticeably lower than that of Co-Ni-S-Se (311 mV). The Tafel slope of Co-Ni-Ru-S-Se (1:1:0.5:1:1) was 52.2 mV dec^{-1}, which was also better than that of the Co-Ni-S-Se catalyst (76.3 mV dec^{-1}) (Fig. 5b), demonstrating the rapid OER rate of Co-Ni-Ru-S-Se (1:1:0.5:1:1). Moreover, the ECSA of the samples could be reflected from the value of C_{dl}. The C_{dl} (Figs. S8, S9) of the Co-Ni-Ru-S-Se catalyst (12.15 mF cm^{-2}) was superior to those of the Co-Ni-S-Se (11.73 mF cm^{-2}) and Co-Ru-S-Se (4.13 mF cm^{-2}) catalysts. The other C_{dl} values of the bimetallic composite materials are shown in Figs. S10, S11. The large ECSA of Co-Ni-Ru-S-Se could be ascribed to the increased number of active sites via the doped atoms, demonstrating the distinct catalytic performance of Co-Ni-Ru-S-Se. EIS measurements were also carried out to better illustrate the enhanced performance of Co-Ni-Ru-S-Se. The EIS plots revealed that the Co-Ni-Ru-S-Se catalyst exhibited a smaller semicircle diameter (Fig. 5d). This result demonstrated that Ru and Ni doping could greatly decrease the impedance, thus giving rise to a preferable R_{ct} of Ru and Ni incorporation in alkaline media. The obtained η_{10} of Co-Ni-Ru-S-Se (1:1:0.5:1:1) was better than those of previously well-known catalysts prepared in alkaline media (Fig. 5e). This phenomenon revealed that doping with Ru and Ni atoms and the incorporation of Co-S-Se could greatly improve the OER reactivity. The overpotential of the Co-Ni-Ru-S-Se catalysts remained continuously stable after 48 h of measurement under a current density of 10 mA cm^{-2}, thereby demonstrating their favorable stability. The TEM image (inset in Fig. 5f) confirmed that the morphology of Co-Ni-Ru-S-Se was well preserved with negligible changes; thus, Co-Ni-Ru-S-Se accounted for the structural durability of the Co-Ni-Ru-S-Se catalyst. Furthermore, the preferable stability of Co-Ni-Ru-S-Se was also examined by XPS spectroscopy, and the interior structure of the electrocatalyst was preserved. According to the XPS spectral results (Fig. S12), the Ni 2p peaks after the OER process were still found at 855.6 and 874.1 eV, which is in accordance with Ni $2p_{3/2}$ and Ni $2p_{1/2}$ in Co-Ni-Ru-S-Se in the early unreacted stage, respectively. The Co $2p_{3/2}$ spectrum after the OER test also showed two spin-orbit peaks. The Co $2p_{3/2}$ peaks were assigned to Co(III) (779.47 eV) and Co(II) (795.97 eV) and accompanied by a satellite peak (788.32 eV), which was assigned to the Co in Co-Ni-Ru-S-Se with only a slight displacement. In our case, the observed Ru 3p spectrum after the OER process designated the Ru $3p_{3/2}$ peak of Co-Ni-Ru-S-Se was Ru(IV) (464.10 eV). The XPS spectrum and TEM spectrum both confirmed the material stability regarding its structure and activity. This phenomenon further confirmed the excellent stability of the Co-Ni-Ru-S-Se catalyst. The distinguished OER electrocatalytic performance of the Co-Ni-Ru-S-Se nanosheets could thus be ascribed to the appropriate chemical constitutions and structural morphologies.

Electrocatalytic enhancement mechanism

To explore the typical mechanism underlying the outstanding OER properties of Co-Ni-Ru-S-Se, crystal structures of Co-Ni-Ru-S-Se, Co-Ni-S-Se, and Co-Ru-S-Se were built (Fig. 6a–c)[59,60]. DFT studies were executed to determine the effects of Co-Ru-S-Se and Co-Ni-S-Se on the atomic-level electronic structure[61] as shown by the DOS of the bimetal calculated in Fig. 6d, e[62]. After the elements Ni and Ru were simultaneously doped into the Co-S-Se framework, the DOS of Co-Ni-Ru-S-Se was greatly increased compared with Co-Ru-S-Se and Co-Ni-S-Se,

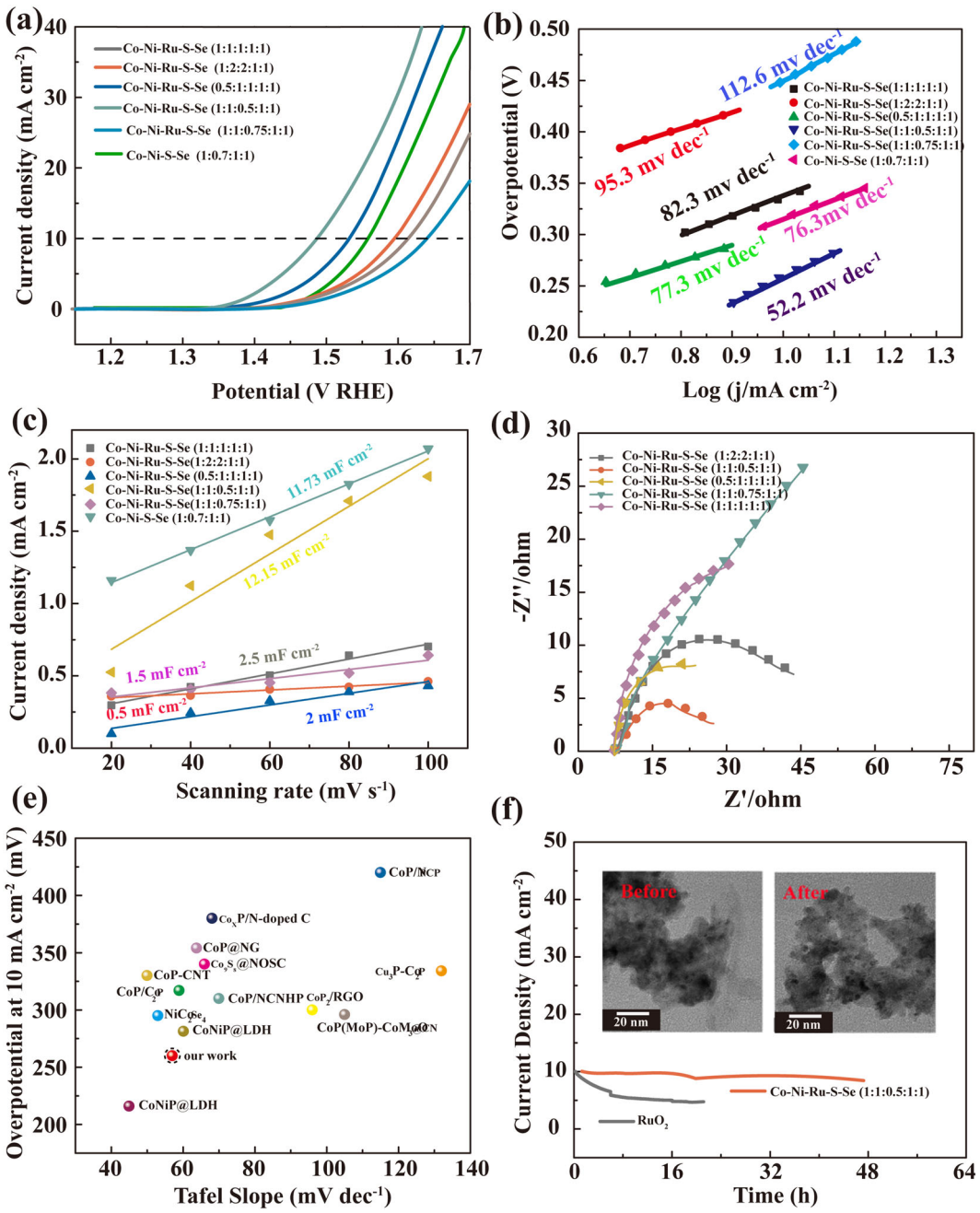

Fig. 5 Electrocatalytic OER properties of the trimetallic Co-Ni-Ru-S-Se nanosheets. a OER polarization curves. **b** Tafel plots of Co-Ni-Ru-S-Se and Co-Ni-S-Se. **c** C_{dl} values of current density differences plotted against scan rates of Co-Ni-Ru-S-Se and Co-Ni-S-Se. **d** EIS Nyquist plots of Co-Ni-Ru-S-Se. **e** Tafel slopes and overpotentials of Co-Ni-Ru-S-Se compared with other OER catalysts. **f** Long-term stability measurement for the Co-Ni-Ru-S-Se at current densities of 10 mA cm^{-2} for 48 h, the inset showed the TEM images before and after the stability measurement for OER.

respectively (Fig. 6f). The high DOS of Co-Ni-Ru-S-Se illustrated that more electron transport occurred and subsequently accelerated the electrocatalytic reaction, which contributed significantly to enhancing the OER performance[63,64]. In addition, the DOS intensity was closely associated with the electric conductivity. The faster charge transfer kinetics of Co-Ni-Ru-S-Se are due to the increased DOS intensity, which shows close agreement with the charge transfer resistance. Therefore, simultaneous Ru and Ni atom doping provides even more catalytic active sites to achieve OH adsorption, which is vital for successful oxygen release.

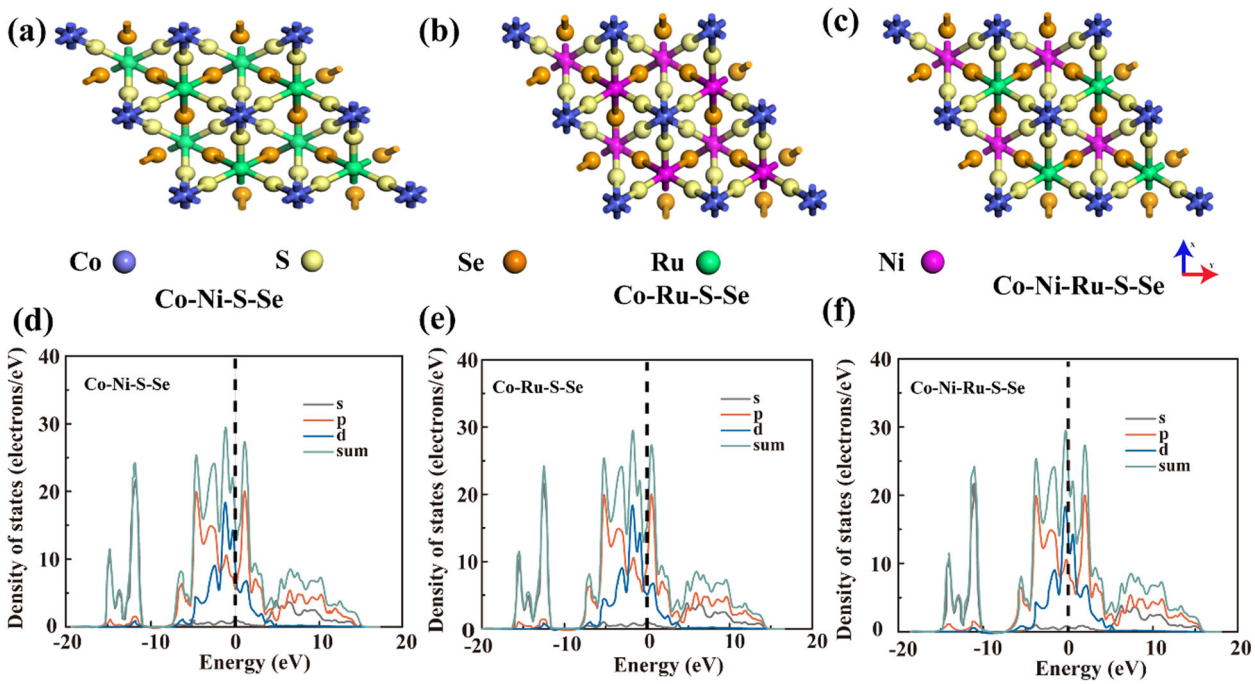

Fig. 6 DFT calculated density of states (DOS) with corresponding optimized structures. Structure representations of **a** Co-Ni-S-Se, **b** Co-Ru-S-Se, **c** Co-Ni-Ru-S-Se. **d**–**f** their calculated DOS, the black dotted line marks the DOS at Fermi level.

DFT was utilized to calculate the adsorption Gibbs free energy (ΔG) of Co-Ni-Ru-S-Se to clarify the reason for the material's outstanding OER properties in alkaline media[65,66]. We built a series of theoretical structure models (Figs. S13–S15) and probed the OER mechanism through a four-electron transfer process (Fig. 7a). Under such conditions, the ΔG values of the different steps (OH*, O*, and OOH*) were selected to illuminate the active electrocatalytic mechanism[67,68]. The theoretical initial potentials for the OER on Co-Ni-S-Se, Co-Ru-S-Se, and Co-Ni-Ru-S-Se were calculated by Equation S3. The step with the maximum ΔG_n value for the four-electron process is the rate-determining step (RDS)[69]. The free energy profiles of the OER on Co-Ru-S-Se and Co-Ni-S-Se indicated that the RDS was the one-step formation of OOH*, giving ΔG_n values of 1.79 eV and 1.71 eV, respectively, which were in accordance with the transformation overpotentials of 560 and 480 mV (Fig. 7b, c). Nevertheless, the free energy of Co-Ni-Ru-S-Se (Fig. 7d) changed to 1.60 eV, which was equivalent to an overpotential of 370 mV. After simultaneous Ru and Ni doping, the OER activity of the catalysts increased. More importantly, the charge density distribution diagrams of Co-Ni-S-Se, Co-Ru-S-Se, and Co-Ni-Ru-S-Se (Fig. 7e–g) showed that the simultaneous doping of Ru and Ni atoms aggravated the unevenness of the charge distribution. The Co site represents the center of the lack of electrons and is considered to be a superior activation site to achieve OH adsorption. Therefore, Ru and Ni simultaneously doped into hybrid materials could introduce an increased number of active catalytic sites for achieving OH adsorption, which has shown vital advantages for successful oxygen release.

Conclusion

A new multi-metal hybrid material-doped Co-S-Se nanocomposite was designed via a one-step hydrothermal method using $Co(acac)_3$, S, Se, and other metal ions (Ni, Ru, Cd, and Au). Compared with bimetallic Co-Ni-S-Se, Co-Ru-S-Se, Co-Au-S-Se and Co-Cd-S-Se nanosheets, the obtained trimetallic Co-Ni-Ru-S-Se nanosheets possessed high conductivity, gave an abundance of metallic active sites, and provided close contact between the nonmetal and metal, thus contributing to high activity, quick electron transport, the facile release of produced bubbles and outstanding durability for the electrocatalytic reaction. Therefore, Co-Ni-Ru-S-Se exhibits superior OER catalytic activity in alkaline solution and possesses outstanding prospects for the electrolysis of water. Furthermore, the commonly used composite strategy paves the way for the extensive preparation of polymetallic sulfoselenide catalysts with accurately steerable morphologies and electronic configurations, bringing about wider applications.

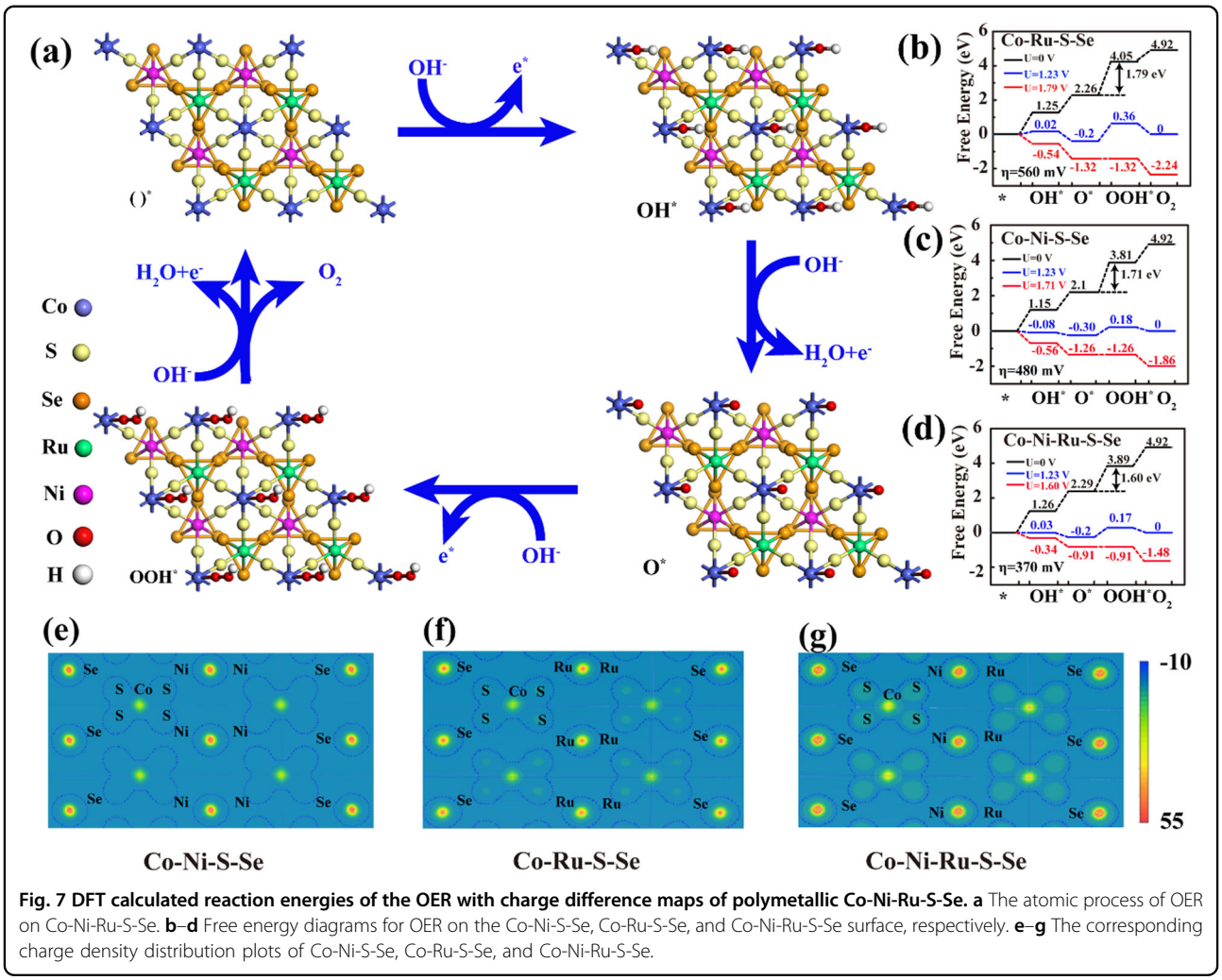

Fig. 7 DFT calculated reaction energies of the OER with charge difference maps of polymetallic Co-Ni-Ru-S-Se. a The atomic process of OER on Co-Ni-Ru-S-Se. **b**–**d** Free energy diagrams for OER on the Co-Ni-S-Se, Co-Ru-S-Se, and Co-Ni-Ru-S-Se surface, respectively. **e**–**g** The corresponding charge density distribution plots of Co-Ni-S-Se, Co-Ru-S-Se, and Co-Ni-Ru-S-Se.

Acknowledgements
The research was sponsored by the Natural Science Foundation of China (grant nos. 21805068, 21976123), the Shanghai University Young Teacher Training Program (grant no. ZZyy16010), and the Shanghai Municipal Peak Plateau Construction Program (grant 1021ZK191601008-A21). The authors would like to thank Nannan Han from the Shiyanjia Lab (www.shiyanjia.com) for carrying out the XPS analysis. F.J. and W.D. thank the computing resources at the Super-computational Center of the QIBEBT.

Author contributions
F.J. and W.D. designed the experiments. W.X. and D.L. performed material characterization analysis. Y.G. and Z.C. analyzed the material characterization results. J.Y. performed the electrochemical measurements and analyzed the obtained results. R.Y. provided detailed structures of the OER intermediates through DFT calculations. W.D. wrote the manuscript. F.J., W.D., X.B., and R.Y. revised the manuscript. All authors discussed the results and commented on the manuscript.

Competing interests
The authors declare no competing interests.

Publisher's note
Springer Nature remains neutral with regard to jurisdictional claims in published maps and institutional affiliations.

Supplementary information The online version contains supplementary material available at https://doi.org/10.1038/s41427-022-00373-9.

Received: 27 October 2021 Revised: 6 February 2022 Accepted: 15 February 2022.
Published online: 18 March 2022

References

1. Xiao, Y. et al. Regulating the pore structure and oxygen vacancies of cobaltosic oxide hollow dodecahedra for an enhanced oxygen evolution reaction. *NPG Asia Mater.* **12**, 73 (2020).
2. Wang, M. H. et al. Bimetallic NiCo metal-organic frameworks for efficient non-Pt methanol electrocatalytic oxidation. *Appl. Catal. A: Gen.* https://doi.org/10.1016/j.apcata.2021.118159 (2021).
3. Kwon, N. H. et al. A rational method to kinetically control the rate-determining step to explore efficient electrocatalysts for the oxygen evolution reaction. *NPG Asia Mater.* **10**, 659–669 (2018).
4. Ahmed, A. T. A., Pawar, S. M., Inamdar, A. I., Kim, H. & Im, H. A morphologically engineered robust bifunctional $CuCo_2O_4$ nanosheet catalyst for highly efficient overall water splitting, *Adv. Mater. Interfaces* https://doi.org/10.1002/admi.201901515 (2020).
5. Wu, Y. Z. et al. Orienting active crystal planes of new class lacunaris Fe_2PO_5 polyhedrons for robust water oxidation in alkaline and neutral media. *Adv. Funct. Mater.* https://doi.org/10.1002/adfm.201801397 (2018).

6. Anandhababu, G., Huang, Y. Y., Babu, D. D., Wu, M. X. & Wang, Y. B. Oriented growth of ZIF-67 to derive 2D porous CoPO nanosheets for electrochemical-/photovoltage-driven overall water splitting, *Adv. Funct. Mater.* https://doi.org/10.1002/adfm.201706120 (2018).
7. Meijiao, Q. et al. Regulating electron density of NiFe-P nanosheets electrocatalysts by a trifle of Ru for high-efficient overall water splitting. *Appl. Catal. B: Environ.* https://doi.org/10.1016/j.apcatb.2019.118324 (2019).
8. Gupta, S. et al. Approaching barrier-free contacts to monolayer MoS_2 employing [Co/Pt] multilayer electrodes. *NPG Asia Mater.* **13**, 13 (2021).
9. Aiqun, K. et al. Synergetic control of Ru/MXene 3D electrode with superhydrophilicity and superaerophobicity for overall water splitting. *Chem. Eng. J.* https://doi.org/10.1016/j.cej.2021.131234. (2021).
10. Koyama, C. et al. Very sharp diffraction peak in nonglass-forming liquid with the formation of distorted tetraclusters. *NPG Asia Mater.* **12**, 43 (2020).
11. Jiang, F., Choy, W. C. H., Li, X. C., Zhang, D. & Cheng, J. Q. Post-treatment-free solution-processed non-stoichiometric NiOx nanoparticles for efficient hole-transport layers of organic optoelectronic devices. *Adv. Mater.* **27**, 2930–2937 (2015).
12. Shao, Z. Y. et al. Boosting electrocatalysis by heteroatom doping and oxygen vacancies in hierarchical Ni-Co based nitride phosphide hybrid. *J. Power Sources* **422**, 33–41 (2019).
13. Wang, N. et al. Activity enhancement via borate incorporation into a NiFe (oxy) hydroxide catalyst for electrocatalytic oxygen evolution. *J. Mater. Chem. A* **6**, 16959–16964 (2018).
14. Zhang, H. B., Zhou, W., Dong, J. C., Lu, X. F. & Lou, X. W. Intramolecular electronic coupling in porous iron cobalt (oxy)phosphide nanoboxes enhances the electrocatalytic activity for oxygen evolution. *Energy Environ. Sci.* **12**, 3348–3355 (2019).
15. Huang, P. et al. Crystalline chirality and interlocked double hourglass Weyl fermion in polyhedra-intercalated transition metal dichalcogenides. *NPG Asia Mater.* **13**, 49 (2021).
16. Chen, Z. D. et al. Construction of CoNiSSe-g-C_3N_4 nanosheets with high exposed conductive interface for boosting oxygen evolution reaction. *J. Alloy. Compd.* **887**, 161346 (2021).
17. Meng, K. et al. Vanadium nitride based CoFe Prussian blue analogues for enhanced electrocatalytic oxygen evolution. *Int. J. Hydrog. Energy* **45**, 31410–31417 (2020).
18. Denny, S. R., Tackett, B. M., Tian, D., Sasaki, K. & Chen, J. G. Exploring electrocatalytic stability and activity of unmodified and platinum-modified tungsten and niobium nitrides. *Int. J. Hydrog. Energy* **45**, 22883–22892 (2020).
19. Read, C. G., Callejas, J. F., Holder, C. F. & Schaak, R. E. General strategy for the synthesis of transition metal phosphide films for electrocatalytic hydrogen and oxygen evolution. *Acs Appl. Mater. Interfaces* **8**, 12798–12803 (2016).
20. Wang, C. S. et al. Tailoring the nanostructure and electronic configuration of metal phosphides for efficient electrocatalytic oxygen evolution reactions,. *Nano Energy* **69**, 104453 (2020).
21. Wang, B. L. et al. Heat diffusion-induced gradient energy level in multishell bisulfides for highly efficient photocatalytic hydrogen production. *Adv. Energy Mater.* **10**, 2001575 (2020).
22. Zhou, Y. N. et al. Carbon-based transition metal sulfides/selenides nanostructures for electrocatalytic water splitting. *J. Alloy. Compd.* **852**, 156810 (2021).
23. Cao, B. et al. Tailoring the d-band center of N-doped carbon nanotube arrays with Co_4N nanoparticles and single-atom Co for a superior hydrogen evolution reaction. *NPG Asia Mater.* **13**, 1 (2021).
24. Yang, J. et al. A universal strategy to metal wavy nanowires for efficient electrochemical water splitting at pH-universal conditions, *Adv. Funct. Mater.* https://doi.org/10.1002/adfm.201803722 (2018).
25. Jiang, F. et al. A facile approach to prepare a microporous polycarbazole P-tetra(4-(N-carbazolyl)phenyl)silane network with high CO_2 storage and separation properties. *N. J. Chem.* **40**, 4969–4973 (2016).
26. Snapp, P. et al. Interaction of 2D materials with liquids: wettability, electrochemical properties, friction, and emerging directions. *NPG Asia Mater.* **12**, 22 (2020).
27. Wang, C. & Qi, L. M. Heterostructured inter-doped ruthenium-cobalt oxide hollow nanosheet arrays for highly efficient overall water splitting. *Angew. Chem. Int. Ed.* **59**, 17219–17224 (2020).
28. Jaouhari, A. E. et al. The role of selenium vacancies in the enhancement of electrocatalytic activity of $CoNiSe_2$ for the oxygen evolution reaction,. *J. Power Sources* **514**, 230596–230606 (2021).
29. Chen, T. & Tan, Y. Hierarchical CoNiSe2 nano-architecture as a high-performance electrocatalyst for water splitting. *Nano Res.* **11**, 1331–1344 (2018).
30. Yang, Y. et al. CoNiSe2 heteronanorods decorated with layered-double-hydroxides for efficient hydrogen evolution. *Appl. Catal. B-Environ.* **242**, 132–139 (2019).
31. Jansi Rani, B. et al. $CoNiSe_2$ nanostructures for clean energy production. *ACS Omega* **5**, 14702–14710 (2020).
32. Yan, L. T. et al. Metal-organic frameworks derived nanotube of nickel-cobalt bimetal phosphides as highly efficient electrocatalysts for overall water splitting. *Adv. Funct. Mater.* **27**, 1703455 (2017).
33. Zhuang, L. Z. et al. Defect-induced Pt-Co-Se coordinated sites with highly asymmetrical electronic distribution for boosting oxygen-involving electrocatalysis. *Adv. Mater.* **31**, 1805581 (2019).
34. Kim, B. H. et al. Metallic phase transition metal dichalcogenide quantum dots showing different optical charge excitation and decay pathways. *NPG Asia Mater.* **13**, 41 (2021).
35. Doan, T. L. L. et al. Hierarchical three-dimensional framework interface assembled from oxygen-doped cobalt phosphide layer-shelled metal nanowires for efficient electrocatalytic water splitting. *Appl. Catal. B-Environ.* **261**, 118268 (2020).
36. Li, M. X., Liu, Z. H., Zha, Q. Q., Li, S. F. & Ni, Y. H. Non-precious metal nanotube arrays hybrid catalyst prepared by a mutual template method for efficient water oxidation in alkaline medium. *Chem. Eng. J.* **410**, 128330 (2021).
37. Sun, J. Q. et al. Molecular engineering of Ni-/Co-porphyrin multilayers on reduced graphene oxide sheets as bifunctional catalysts for oxygen evolution and oxygen reduction reactions. *Chem. Sci.* **7**, 5640–5646 (2016).
38. Kim, Y. J. & Yang, C. H. Electret formation in transition metal oxides by electrochemical amorphization. *NPG Asia Mater.* **12**, 1 (2020).
39. Zhou, Q. et al. Active-site-enriched iron-doped nickel/cobalt hydroxide nanosheets for enhanced oxygen evolution reaction. *Acs Catal.* **8**, 5382–5390 (2018).
40. Gao, F., Zhang, Y. P., Wu, Z. Y., You, H. M. & Du, Y. K. Universal strategies to multi-dimensional noble-metal-based catalysts for electrocatalysis. *Coord. Chem. Rev.* **436**, 213825–213847 (2021).
41. Zhang, Y. P. et al. Recent advances in one-dimensional noble-metal-based catalysts with multiple structures for efficient fuel-cell electrocatalysis. *Coord. Chem. Rev.* **450**, 214244–214262 (2022).
42. Gao, F., Zhang, Y. P., Ren, F. F., Shiraishi, Y. & Du, Y. K. Universal surfactant-free strategy for self-standing 3D tremella-like Pd-M (M=Ag, Pb, and Au) nanosheets for superior alcohols electrocatalysis. *Adv. Funct. Mater.* **30**, 2000255–2000263 (2020).
43. Gao, F. et al. Shape-control of one-dimensional PtNi nanostructures as efficient electrocatalysts for alcohol electrooxidation. *Nanoscale* **11**, 4831–4836 (2019).
44. Zhuang, L. H. et al. Ultrathin iron-cobalt oxide nanosheets with abundant oxygen vacancies for the oxygen evolution reaction. *Adv. Mater.* **29**, 1606793 (2017).
45. Cao, D. F. et al. Engineering the in-plane structure of metallic phase molybdenum disulfide via Co and O dopants toward efficient alkaline hydrogen evolution. *ACS Nano* **13**, 11733–11740 (2019).
46. Guo, Y. Y. et al. Carbon nanosheets containing discrete Co-N-x-B-y-C active sites for efficient oxygen electrocatalysis and rechargeable Zn-Air batteries. *ACS Nano* **12**, 1894–1901 (2018).
47. Ren, H. et al. Amorphous Fe-Ni-P-B-O nanocages as efficient electrocatalysts for oxygen evolution reaction. *ACS Nano* **13**, 12969–12979 (2019).
48. Duan, H. T. et al. Non-stoichiometric NiOx nanocrystals for highly efficient electrocatalytic oxygen evolution reaction. *J. Electroanalytical Chem.* **885**, 114966 (2021).
49. Wu, Q. L. et al. Identifying electrocatalytic sites of the nanoporous copper-ruthenium alloy for hydrogen evolution reaction in alkaline electrolyte. *ACS Energy Lett.* **5**, 192–199 (2020).
50. Wang, F. X. et al. A stimulus-responsive zinc-iodine battery with smart overcharge self-protection function. *Adv. Mater.* **32**, 2000287 (2020).
51. Zhang, L. S. et al. Boosting neutral water oxidation through surface oxygen modulation. *Adv. Mater.* **32**, 2002297 (2020).
52. Zhang, Y. et al. A 3D multi-interface structure of coral-like Fe-Mo-S/Ni3S2@NF using for high-efficiency and stable overall water splitting. *Chem. Eng. J.* **404**, 126483 (2021).
53. Wu, D., Hao, J., Song, Z. X., Fu, X. Z. & Luo, J. L. All roads lead to Rome: an energy-saving integrated electrocatalytic CO_2 reduction system for concurrent value-added formate production. *Chem. Eng. J.* **412**, 127893 (2021).

54. Yin, J. et al. NiO/CoN porous nanowires as efficient bifunctional catalysts for Zn-Air batteries. *ACS Nano* **11**, 2275–2283 (2017).
55. Zhao, L. et al. Interdiffusion reaction-assisted hybridization of two-dimensional metal-organic frameworks and Ti3C2Tx nanosheets for electrocatalytic oxygen evolution. *ACS Nano* **11**, 5800–5807 (2017).
56. Fang, G. Z. et al. Metal organic framework-templated synthesis of bimetallic selenides with rich phase boundaries for sodium-ion storage and oxygen evolution reaction, *ACS Nano* **13**, 5635–5645 (2019).
57. Kim, J. et al. Synergistic coupling derived cobalt oxide with nitrogenated holey two-dimensional matrix as an efficient bifunctional catalyst for metal-air batteries. *ACS Nano* **13**, 5502–5512 (2019).
58. Hua, B. et al. The excellence of both worlds: developing effective double perovskite oxide catalyst of oxygen reduction reaction for room and elevated temperature applications. *Adv. Funct. Mater.* **26**, 4106–4112 (2016).
59. Wang, Q. L. et al. Coordination engineering of iridium nanocluster bifunctional electrocatalyst for highly efficient and pH-universal overall water splitting. *Nat. Commun.* **11**, 4246 (2020).
60. Gao, J. J. et al. Breaking long-range order in iridium oxide by alkali ion for efficient water oxidation. *J. Am. Chem. Soc.* **141**, 3014–3023 (2019).
61. Zhang, Y. et al. Nanostructured metal chalcogenides for energy storage and electrocatalysis. *Adv. Funct. Mater.* **27**, 1702317 (2017).
62. Kuang, M. et al. Electronic tuning of Co, Ni-based nanostructured (Hydr) oxides for aqueous electrocatalysis. *Adv. Funct. Mater.* **28**, 1804886 (2018).
63. Qiu, B. C. et al. Fabrication of nickel-cobalt bimetal phosphide nanocages for enhanced oxygen evolution catalysis. *Adv. Funct. Mater.* **28**, 1706008 (2018).
64. Amiinu, I. S. et al. From 3D ZIF nanocrystals to Co-N-x/C nanorod array electrocatalysts for ORR, OER, and Zn-Air batteries. *Adv. Funct. Mater.* **28**, 1704638 (2018).
65. Pan, J. B. et al. Activity and stability boosting of an oxygen-vacancy-rich BiVO4 photoanode by NiFe-MOFs thin layer for water oxidation. *Angew. Chem.-Int. Ed.* **60**, 1433–1440 (2021).
66. Cao, E. P. et al. Boron-induced electronic-structure reformation of CoP nanoparticles drives enhanced pH-universal hydrogen evolution. *Angew. Chem.-Int. Ed.* **59**, 4154–4160 (2020).
67. Hui, L. et al. Overall water splitting by graphdiyne-exfoliated and -sandwiched layered double-hydroxide nanosheet arrays. *Nat. Commun.* **9**, 5309 (2018).
68. Xu, W. C. et al. A-site excessive (La0.8Sr0.2)(1+x)MnO3 perovskite oxides for bifunctional oxygen catalyst in alkaline media. *ACS Catal.* **9**, 5074–5083 (2019).
69. Wu, Y. Q. et al. Cr-doped FeNi-P nanoparticles encapsulated into N-doped carbon nanotube as a robust bifunctional catalyst for efficient overall water splitting. *Adv. Mater.* **31**, 1900178 (2019).